SCIENTIFIC REPORTS

natureresearch

OPEN

Fabrication of porous NiMn$_2$O$_4$ nanosheet arrays on nickel foam as an advanced sensor material for non-enzymatic glucose detection

Jie Zhang[1], Yudong Sun[2], Xianchun Li[1]* & Jiasheng Xu[2]*

In this work, porous NiMn$_2$O$_4$ nanosheet arrays on nickel foam (NiMn$_2$O$_4$ NSs@NF) was successfully fabricated by a simple hydrothermal step followed by a heat treatment. Porous NiMn$_2$O$_4$ NSs@NF is directly used as a sensor electrode for electrochemical detecting glucose. The NiMn$_2$O$_4$ nanosheet arrays are uniformly grown and packed on nickel foam to forming sensor electrode. The porous NiMn$_2$O$_4$ NSs@NF electrode not only provides the abundant accessible active sites and the effective ion-transport pathways, but also offers the efficient electron transport pathways for the electrochemical catalytic reaction by the high conductive nickel foam. This synergy effect endows porous NiMn$_2$O$_4$ NSs@NF with excellent electrochemical behaviors for glucose detection. The electrochemical measurements are used to investigate the performances of glucose detection. Porous NiMn$_2$O$_4$ NSs@NF for detecting glucose exhibits the high sensitivity of 12.2 mA mM^{-1} cm^{-2} at the window concentrations of 0.99–67.30 μM (correlation coefficient = 0.9982) and 12.3 mA mM^{-1} cm^{-2} at the window concentrations of 0.115–0.661 mM (correlation coefficient = 0.9908). In addition, porous NiMn$_2$O$_4$ NSs@NF also exhibits a fast response of 2 s and a low LOD of 0.24 μM. The combination of porous NiMn$_2$O$_4$ nanosheet arrays and nickel foam is a meaningful strategy to fabricate high performance non-enzymatic glucose sensor. These excellent properties reveal its potential application in the clinical detection of glucose.

The World Health Organization (WHO) reported that the diabetes and its complications by high glucose concentration in the human body have resulted in approximately 350 million people around world[1–3]. The diabetes will be the 7th, leading cause of death by 2030[3–5]. Development of highly selective and sensitive detection method for glucose detection is of significance in a variety of fields, such as blood glucose testing, foods monitoring and pharmaceutical analysis[5–7]. The conventional techniques, such as colorimetry, chemiluminescence, electro-chemiluminescence and fluorescence are used as determination method for glucose biomolecule[7–10]. With the rapid developments of the electrochemical science and technology, electrochemical sensors have been developed to detect glucose levels due to its combination of performance parameters such as reliable, accurate, sensitive and fast response[10–14].

Sensors for glucose detection, including enzymatic and non-enzymatic detection methods, are the most convenient and promising method due to its sensitivity and reproducibility[15,16]. Enzyme-immobilized glucose sensors suffer from some intrinsic drawbacks such as lack of temperature and pH stability, high cost and low shelf-life[17–19]. The above mentioned drawbacks limit their practical application although they possess high sensitivity and the excellent selectivity[20,21]. Non-enzymatic glucose sensors can avoid the intrinsic drawbacks of enzyme sensor. Non-enzymatic electrochemical glucose sensors possess the advantages over enzymatic sensors in terms of low cost, good thermal stability and satisfactory reproducibility[21,22]. Non-enzymatic electrochemical detection sensor is based on the oxidize glucose to a detectable electrochemical signal, which directly occurs on the electrode surface by an electric current effect[23]. For the non-enzymatic glucose sensor, the design and fabrication of the active materials play a key role in the sensing performances since it can efficiently catalyze and oxidize glucose to produce gluconolactone and can free from the operating conditions[24,25].

[1]School of Chemical Engineering, University of Science and Technology Liaoning, Anshan, 114051, P.R. China. [2]Liaoning Province Key Laboratory for Synthesis and Application of Functional Compounds, College of Chemistry and Chemical Engineering, Bohai University, Jinzhou, 121013, P.R. China. *email: xianchunli@ustl.edu.cn; jiashengxu@bhu.edu.cn
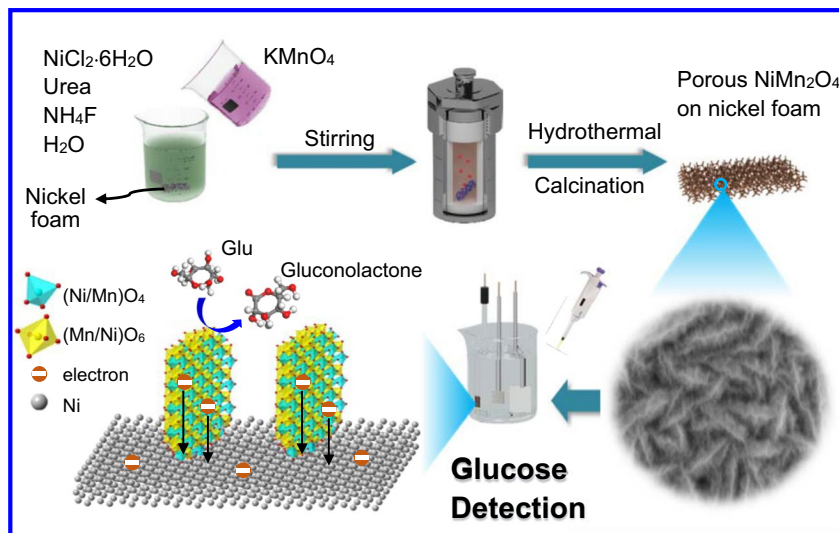
1

Figure 1. Schematic illustrations of the fabrication process for porous $NiMn_2O_4$ NSs@NF sensor electrode.

In recent years, many materials including carbon materials, noble metals, transition metals and transition metal oxides have been widely investigated and used as the active materials in non-enzymatic glucose sensor[26–28]. The poor biocompatibility and low electrical conductivity of carbon materials and high price of noble metals hinder their practical applications[29–31]. Among them, transition metal oxide materials have been extensively explored and researched as electrode materials due to their excellent properties, such as the featured shape dependent, good biocompatibility, non-toxic, electro-catalytic properties and low cost compared with other materials[31–34]. $NiMn_2O_4$, a transition metal oxide with the cubic spinel structure, has attracted attention owing to its high electrical conductivity, good electrochemical performances, abundance in nature, low cost, low toxicity and environmental friendliness. $NiMn_2O_4$ shows a potential as electrode material due to its strong electro-site based on generation of two redox couples of Ni^{2+}/Ni^{3+} and Mn^{3+}/Mn^{4+} in alkaline solution[35,36]. $NiMn_2O_4$ as a promising material will exhibit an excellent electrochemical activity toward the electrochemical detection of glucose.

The design and use of nanomaterials have increasing interest in the fields of glucose detection and sensing[37]. Use of nanostructured materials effectively improves the material characteristics, such as, electron/ion transfer rate, adsorption capability and high loading and immobilization of biomolecules. The nanostructured materials as the ideal candidates overcome drawbacks and limitations and lead to the development of glucose sensor with fast response, high sensitivity and selectivity. For sensors, the active materials intensively depend on the amperometric response of glucose oxidation at the surface of active materials. The nanostructure of the active materials can enlarge the surface-to-volume ratio and enhance the accessible electrochemical reactive sites. The nanostructures also efficiently shorten the transport distance of ions and charges between electrolyte and surface of active materials[38–40]. Thus, developing a nanostructured $NiMn_2O_4$ electrode as non-enzymatic material is of significance to improve the sensing performances of direct glucose detection.

In this work, porous $NiMn_2O_4$ NSs@NF sensor electrode has been designed and fabricated by a facile hydrothermal method followed by a heat treatment. We have chosen 3D nickel foam as electrode substrate for the direct growth of porous $NiMn_2O_4$ nanosheet arrays since nickel foam possesses the advantages of commercial availability, low cost, the excellent electrical conductivity and porous structure, which provides large surface area for the nanostructured construction. This direct grown structure of porous $NiMn_2O_4$ NSs@NF provides unique properties, such as good electron transport, reduced resistance, the excellent electrical conductivity and better adhesion stability compared with non-direct grown electrode. In addition, a synergistic effect between porous $NiMn_2O_4$ nanosheets and the metal substrate enables $NiMn_2O_4$ NSs@NF electrode with the excellent sensing performances for glucose molecules. Porous $NiMn_2O_4$ NSs@NF sensor exhibits a high sensitivity of 12.2 mA mM^{-1} cm^{-2} at the window concentrations of 0.99–67.30 μM and 12.3 mA mM^{-1} cm^{-2} at the window concentrations of 0.115–0.661 mM. Porous $NiMn_2O_4$ NSs@NF electrode also exhibits a low LOD of 0.24 μM as well as the fast response of 2 s. These results suggest that porous $NiMn_2O_4$ NSs@NF is an efficient sensor electrode for glucose detection.

Result and Discussions

Figure 1 illustrates the scheme for the representative fabrication process of porous $NiMn_2O_4$ NSs@NF sensor electrode. The fabrication process of porous $NiMn_2O_4$ NSs@NF electrode includes a hydrothermal process and a heat treatment process. The fabricated porous $NiMn_2O_4$ NSs@NF is directly used as a sensor electrode in the glucose detection system.

XRD patterns are performed to identify the crystallographic structure and the chemical compositions of porous $NiMn_2O_4$ nanosheet arrays ($NiMn_2O_4$ nanosheets are scraped from the nickel foam electrode). XRD patterns of porous $NiMn_2O_4$ NSs@NF are shown in Fig. 2. The diffraction peaks at 2θ values of 18.3°, 30.1°, 35.4°, 37.0°, 43.0°, 53.2°, 56.9°, 62.5°, 73.9° and 74.9° are observed, which can be well indexed to the (111), (220), (311), (222), (400), (422), (511), (440), (533) and (622) planes of the spinel-type $NiMn_2O_4$ phase, respectively. These diffraction peaks can be well indexed to the peaks of the $NiMn_2O_4$ standard diffraction patterns (JCPDS PDF

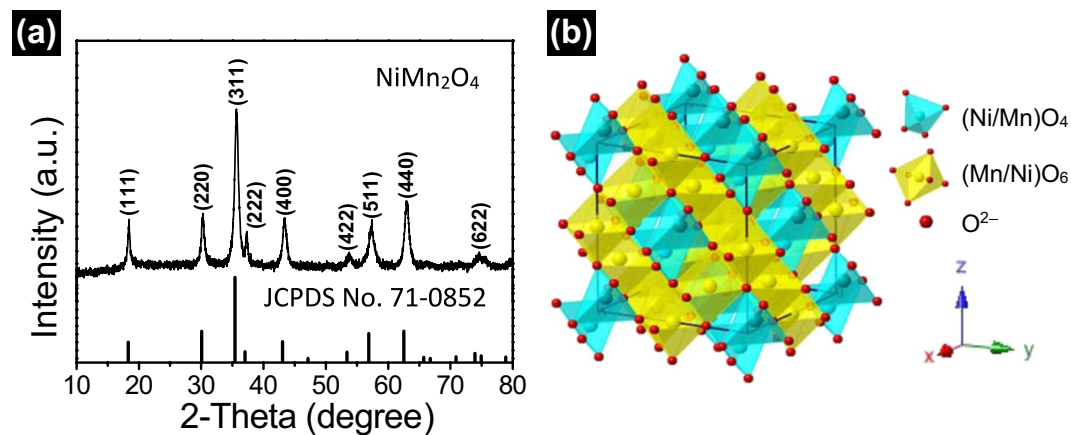**Figure 2.** (**a**) XRD patterns of porous $NiMn_2O_4$ NSs@NF sensor electrode. Several vertical lines at the bottom of XRD patterns is the standard XRD diffraction peaks from JCPDS card No. 71-0852. (**b**) Schematic cystal structure of the spinel $NiMn_2O_4$. Skyblue color tetrahedra denotes the $(Ni/Mn)O_4$ tetrahedra, yellow color octahedra denotes the $(Mn/Ni)O_6$ octahedra.
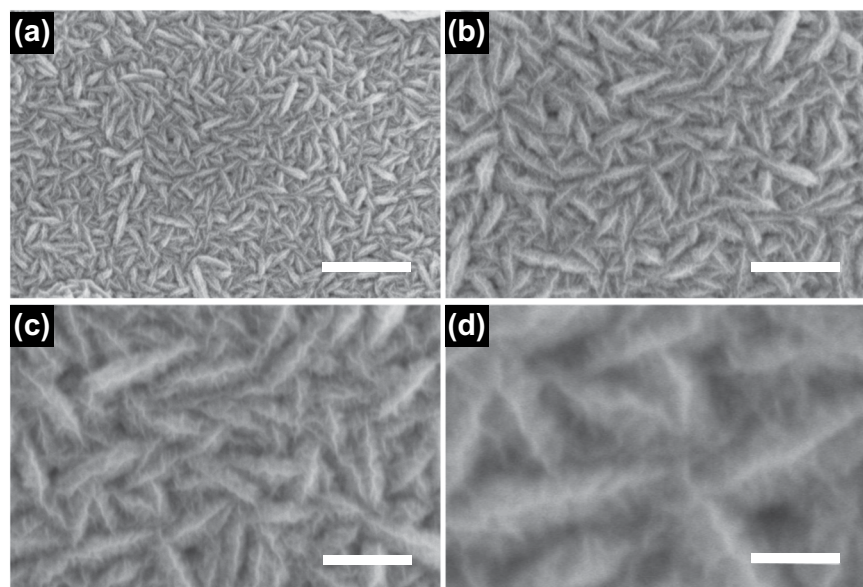

Figure 3. SEM images of porous $NiMn_2O_4$ NSs@NF sensor electrode. (**a**) Low magnification SEM image of porous $NiMn_2O_4$ NSs@NF, scale bars $=1\,\mu m$. (**b,c**) Medium magnification SEM images of porous $NiMn_2O_4$ NSs@NF, scale bars $=500\,\mu m$ and $300\,nm$, respectively. (**d**) High magnification SEM image of porous $NiMn_2O_4$ NSs@NF, scale bars $=100\,nm$.

No. 71-0852, $a = b = c = 8.4\,Å$, space group: cubic $Fd\text{-}3m$(227), $Z = 8$[41], indicating the high purity of $NiMn_2O_4$ phase. These diffraction peaks are broaden in width and weaken in intensity, indicating the low crystallinity of the $NiMn_2O_4$ sample[42]. Figure 2b shows the crystal structure of the spinel $NiMn_2O_4$ sample. Nickel ions and manganese are adopted the cubic structure with mixed valence states for the spinel $NiMn_2O_4$ structure; nickel and manganese occupy randomly but totally proportionally (Ni:Mn $= 1:2$) in the interstices of oxygen stacking tetrahedron and octahedron[43,44]. These cations occupy the cubic lattice composing by close-packed oxygen anions (O^{2-})[45]. For the spinel $NiMn_2O_4$ materials, the low crystalline can improve their electrochemical performances due to numerous of loosely packed atoms being available for redox reaction[46].

The morphology and structure of porous $NiMn_2O_4$ NSs@NF sensor electrode are characterized by SEM. Different magnification SEM images of porous $NiMn_2O_4$ NSs@NF are shown in Fig. 3. Low magnification SEM image shows a panoramic view (Fig. 3a). Porous $NiMn_2O_4$ nanosheets are completely and uniformly coated on surface of nickel foam substrate. Porous $NiMn_2O_4$ nanosheets and nickel foam substrate form an open arrays structure composed of numerous $NiMn_2O_4$ nanoparticles with uniform size. Figure 3b,c show medium magnification SEM images of porous $NiMn_2O_4$ NSs@NF. From Fig. 3b, the porous $NiMn_2O_4$ nanosheets are cross-linked each other and vertically anchored on the surface of nickel foam substrate to form three dimensional ordered

$NiMn_2O_4$ nanosheet arrays. From the Fig. 3c, the length of porous $NiMn_2O_4$ nanosheets is about 250 nm and the breadth of porous $NiMn_2O_4$ nanosheets is about 50 nm. Moreover, the skeleton surface of $NiMn_2O_4$ nanosheets is completely coated by the smaller $NiMn_2O_4$ nanosheets. This hierarchical $NiMn_2O_4@NiMn_2O_4$ core-shell nanosheet nanostructure provides larger surface area, which is capable of facilitating the electrolyte ions diffusion and increasing the contact area between the electrode materials and the electrolyte ions.

Figure 3d shows the high magnification SEM image of porous $NiMn_2O_4$ NSs@NF. These smaller $NiMn_2O_4$ nanosheets growth on surface of $NiMn_2O_4$ nanosheets. In addition, we also can find that these smaller $NiMn_2O_4$ nanosheets are almost vertical to the surface of $NiMn_2O_4$ nanosheet. These smaller $NiMn_2O_4$ nanosheets are wrinkles. The length of these smaller $NiMn_2O_4$ nanosheets is about 20 nm on average. More detailed structures are further shown in Figs. S1–S4. There is space between the smaller $NiMn_2O_4$ nanosheets forming 3D spatial structure, which can facilitate the electrolyte ions diffusion and provide larger surface area for electrocatalytic reactions. The unique 3D core-shell structure greatly reduces distance for the diffusion/transport of electrolyte ions, which can be attributed to the opening structure and excellent performances of $NiMn_2O_4$ nanosheets.

Figure 4 shows TEM and HRTEM images of porous $NiMn_2O_4$ nanosheet arrays (porous $NiMn_2O_4$ nanosheets are scratched from nickel foam consisted of stacking nanosheets). Figure 4a displays a low magnification TEM image. An overall contour of $NiMn_2O_4$ nanosheet is observed in the low magnification TEM image. From this low magnification TEM image, the length and width of this porous $NiMn_2O_4$ nanosheet can be clearly seen about 600 nm and 400 nm, respectively. Figure 4b shows medium magnification TEM image. Medium magnification TEM image further shows the unique core-shell structure of the $NiMn_2O_4$ nanosheet arrays. Figure 4c shows high magnification TEM image. This unique core-shell structure can be clearly observed in high magnification TEM image. These smaller $NiMn_2O_4$ nanosheets, called as "shell" nanosheets, are distributed uniformly on the surface of the "core" $NiMn_2O_4$ nanosheet. Some "shell" $NiMn_2O_4$ nanosheets are marked by the yellow dash line in Fig. 4c. The thickness of the "shell" $NiMn_2O_4$ nanosheets is about 10 nm. This core-shell structure can effectively provide lager surface area and markedly shorten the ion diffusion distance[47]. Figures S5–S7 shows more detailed structures.

Figure 4d,e show the typical high resolution TEM (HRTEM) images of porous $NiMn_2O_4$ nanosheet. Two lattice fringes with the interplanar d-spacing of the 4.88 and 2.49 Å (marked by white) are observed in Fig. 4d, which can be well indexed to the (111) and (222) planes of $NiMn_2O_4$, respectively. Figure 4e also shows two lattice fringes with the d-spacing of the 4.88 and 2.53 Å, which are well indexed to the (111) and (311) planes of $NiMn_2O_4$, respectively. These lattice fringes are agrees well with the XRD patterns (Fig. 2). The selected area electron diffraction (SAED) patterns of porous $NiMn_2O_4$ nanosheet are shown in Fig. 4f. The SAED patterns are composed of several light diffraction circles. Four major diffraction circles can be observed on the SAED patterns. These major diffraction circles clearly match with the (444), (622), (400) and (311) planes of porous $NiMn_2O_4$ nanosheet, respectively, representing the existence of porous $NiMn_2O_4$ nanosheet and its polycrystalline structure[48].

To further analyze the elemental composition and oxidation state, porous $NiMn_2O_4$ NSs@NF sensor electrode is characterized by XPS and the results are analyzed with based on Gaussian-Lorentzian fitting method. Figure 5a displays the full XPS survey spectra of porous $NiMn_2O_4$ NSs@NF electrode, which mainly contains the elements of Ni, Mn and O. Figure 5b shows the Ni spectrum of porous $NiMn_2O_4$ NSs@NF electrode. Two peaks with the binding energies at 853.9 and 855.4 eV correspond to the Ni 2p 3/2[49,50]. The peak at 872.6 eV corresponds to the Ni 2p 1/2[51]. Two peaks with the binding energies located at 860.9 and 879.3 eV as shown in Fig. 5b are the satellite (Sat.) peaks of the Ni 2p 3/2 and Ni 2p 1/2, respectively[52]. Figure 5c shows Mn spectrum of porous $NiMn_2O_4$ NSs@NF electrode. Two spin-orbit peaks in Mn spectrum are deconvolved into four peaks. Two deconvolved peaks are observed at 641.0 and 642.5 eV, which correspond to Mn 2p 3/2. Two deconvolved peaks are observed at 654.0 and 652.6 eV, corresponding to Mn 2p 1/2, which is consistent with the previous reported literature[53]. Two deconvolved peaks are observed at 641.0 and 652.6 eV, which correspond to the correlative peaks of Mn^{2+}; two deconvolved peaks are observed at 642.5 and 654.0 eV, which correspond to the correlative peaks of Mn^{3+} binding energy[54]. Figure 5d shows the O spectrum of porous $NiMn_2O_4$ NSs@NF electrode. The resolved peak at binding energy of 529.4 eV is indexed to typical metal oxygen bonds (M-O-M) or the lattice oxygen[55–57]. The peak for O 1s at 530.6 eV is attributed to metal-O-H from metal surface hydroxyl groups[33,58]. The peak at 531.6 eV is attributed to a larger number of defect sites with a low oxygen coordination normally observed in materials with small particles[55]. The energy dispersive spectroscopy (EDS) mappings of porous $NiMn_2O_4$ NSs@NF sensor electrode are shown in Fig. S8. These EDS mappings indicate that Ni, Mn and O elements are uniformly distributed on porous $NiMn_2O_4$ nanosheet arrays, which in agreement with XRD and XPS characterizations.

The surface area and porosity are two important factors, which can critically influence the sensing performances for detection of glucose. The surface area and porosity of the porous $NiMn_2O_4$ NSs@NF sensor electrode is further analyzed by Brunauer–Emment–Teller (BET) nitrogen isothermal adsorption and desorption test. Figure S9 shows a typical BET nitrogen adsorption and desorption isotherms of $NiMn_2O_4$ NSs@NF electrode. Nitrogen adsorption and desorption isotherms are plotted as quantity volume (V_m) on the y-axis and relative pressure (P/P_0) on the x-axis based to BET experimental data. According to the BET test, the BET specific surface area of porous $NiMn_2O_4$ NSs@NF electrode is calculated to be 77.5 $m^2 g^{-1}$. This large specific area can effectively increase the utilization of $NiMn_2O_4$ as an electrochemically active material in the process of glucose electrochemical detection. The adsorption/desorption isotherms also show a hysteresis, which can be classified as a type IV isotherm according to the profile of the hysteresis loop in a range of $0.5 < P/P_0 < 1.0$[59]. Inset in Fig. S9 shows the corresponding pore-size distribution with calculated by the Barrette Joynere Halenda (BJH) method based on BET experimental data. The pore size distribution image shows a wide pore-size distribution characteristic, which can be attributed to the porous nano-structure of $NiMn_2O_4$ NSs@NF electrode. The pore size distribution image presents that the average pore size of $NiMn_2O_4$ NSs@NF electrode is about 9.6 nm. Porous structure of $NiMn_2O_4$
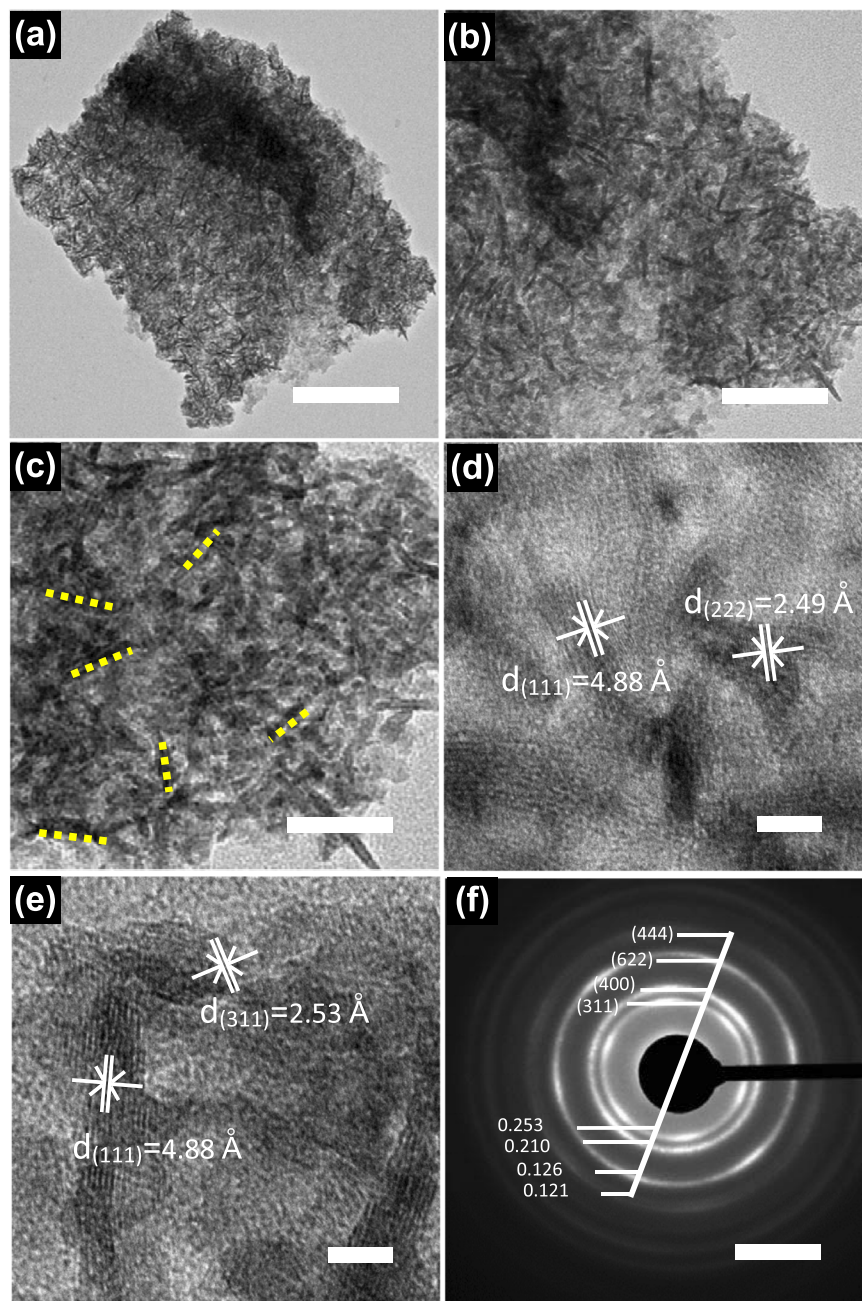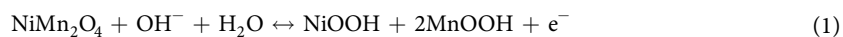
Figure 4. TEM images of porous NiMn$_2$O$_4$ NSs@NF sensor electrode. (**a**) Low magnification TEM image, scale bar = 200 nm; (**b**) Medium magnification TEM image, scale bar = 100 nm; (**c**) High magnification TEM image, scale bar = 50 nm; (**d,e**) High resolution TEM (HRTEM) image of porous NiMn$_2$O$_4$ NSs@NF, scale bar = 5 nm; (**f**) The selected area electron diffraction (SAED) patterns of porous NiMn$_2$O$_4$ NSs@NF, scale bar = 5 1/nm.

NSs@NF electrode with large surface area provides the highway for transportation of electrons and ions between the electrolytes and electrode material, which is in favour of non-enzymatic glucose detection.

Porous NiMn$_2$O$_4$ NSs@NF electrode is used directly as a sensor electrode to test its electrocatalytic activity toward glucose detection in 0.5 M NaOH electrolyte. Figure 6a presents CV curves of porous NiMn$_2$O$_4$ NSs@NF electrode at sweep rate ranging from 10 to 100 mV s^{-1}. Each CV curve displays a pair of redox peak. These peaks in CV curves can be attributed to the electrochemical redox reactions/electrocatalytic oxidation reactions of porous NiMn$_2$O$_4$ NSs@NF electrode. The electrocatalytic oxidation reaction for glucose detection are shown as follows formulae (1–4)[60–62]:
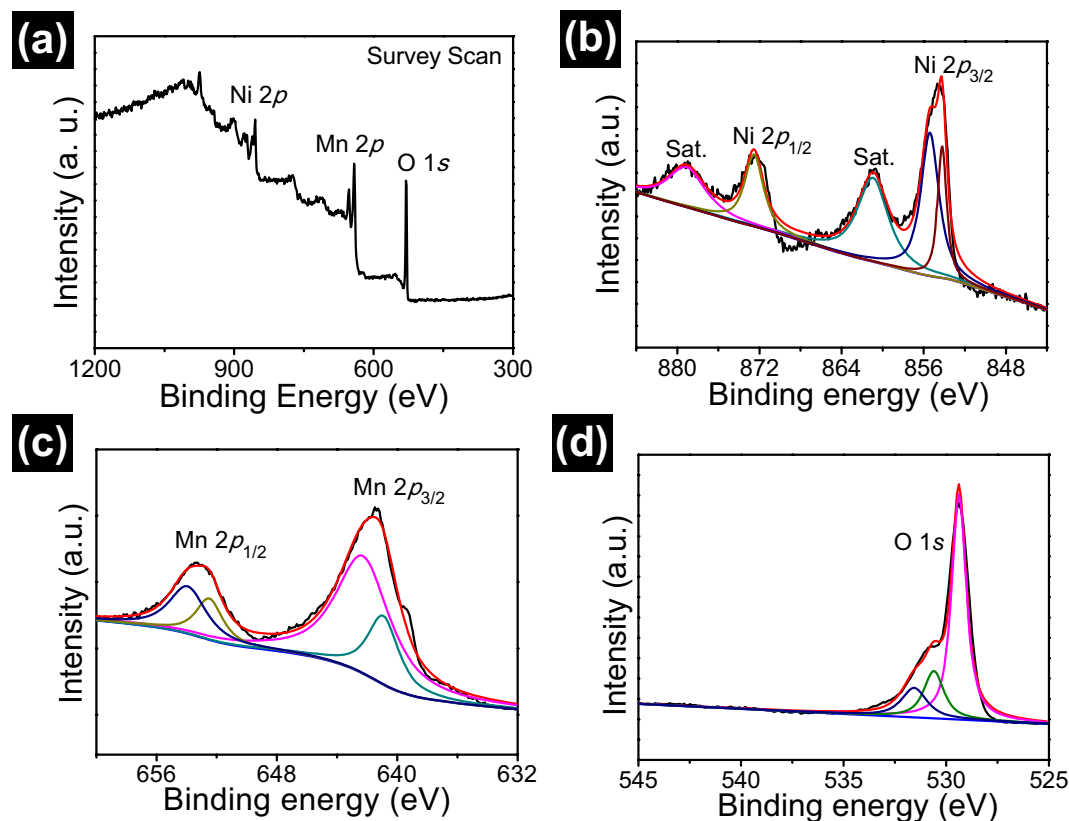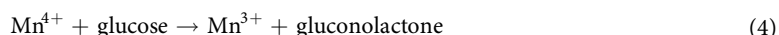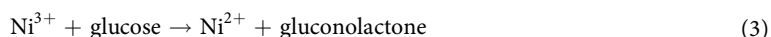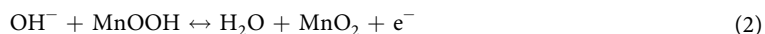
$$NiMn_2O_4 + OH^- + H_2O \leftrightarrow NiOOH + 2MnOOH + e^- \qquad (1)$$

Figure 5. (**a**) X-ray photoelectron spectroscopy (XPS) survey scan spectra of porous $NiMn_2O_4$ NSs@NF sensor electrode. (**b**) Ni $2p$ spectrum. (**c**) Mn $2p$ spectrum. (**d**) O $1s$ spectrum. These black and red curves correspond to the experimental and fitted curves of the spectra of Ni $2p$, Mn $2p$ and O $1s$.

$$OH^- + MnOOH \leftrightarrow H_2O + MnO_2 + e^- \tag{2}$$

$$Ni^{3+} + glucose \rightarrow Ni^{2+} + gluconolactone \tag{3}$$

$$Mn^{4+} + glucose \rightarrow Mn^{3+} + gluconolactone \tag{4}$$

As shown in CV curve at sweep rate of $10\,mV\,s^{-1}$, a pairs of redox peaks at $+0.23/+0.43\,V$ can be observed. With the increase of scan rates, the positive potential shift of the anodic peaks and negative potential shift of cathodic peaks are also observed. The separation of peak to peak ($\triangle Ep$) increases linearly with the increasing scan rates. These phenomena may be attributed to the increase of overpotential[63]. Figure 6b shows the corresponding fitting curves of the response currents vs. the square root of sweep rates. The corresponding fitting curves show the linear dependencies on the sweep rates, indicating that the electron transfer process of electrode is the reversible and diffusion-controlled electrochemical redox process[64].

CV curves of porous $NiMn_2O_4$ NSs@NF sensor electrode at various concentrations of glucose are recorded to investigate the electrochemical sensing performance at the sweep rate of $20\,mV\,s^{-1}$ in a 0.5 M NaOH electrolyte solution. Figure 6c shows CV curves of porous $NiMn_2O_4$ NSs@NF electrode at various concentrations of glucose (from 0 mM to 7 mM). The response currents show a steadily increasing trend with the increase of glucose concentrations. In addition, the response currents of the anodic and cathodic peaks increase with the increase of glucose concentrations. These results indicate good electrochemical sensing performance of porous $NiMn_2O_4$ NSs@NF electrode for glucose. For comparison, the electrochemical behaviors of porous $NiMn_2O_4$ NSs@NF electrode and bare nickel foam for the electrochemical sensing of glucose are investigated by CV technique at the sweep rate of $20\,mV\,s^{-1}$ in a 0.5 M NaOH electrolyte solution. Figure 6d shows CV curves of porous $NiMn_2O_4$ NSs@NF electrode recorded in the presence of glucose and absence of glucose, and CV curve of bare nickel foam in the presence of glucose. The response current obtained on porous $NiMn_2O_4$ NSs@NF electrode with 1 mM glucose is $74.9\,mA\,cm^{-2}$, which is much larger than that obtained on bare nickel foam electrode ($4.6\,mA\,cm^{-2}$). The result indicates the excellent electroactivity of porous $NiMn_2O_4$ NSs@NF electrode towards glucose. In the case of the presence of glucose, porous $NiMn_2O_4$ NSs@NF electrode also exhibits larger closed area than the bare nickel foam, indicating no obvious electrochemical response of bare nickel foam. In addition, porous $NiMn_2O_4$ NSs@NF electrode at the presence of glucose exhibits the high response current ($74.9\,mA\,cm^{-2}$) of the redox peaks compared to those of the absence of glucose ($53.2\,mA\,cm^{-2}$). This result also confirms the good electrochemical
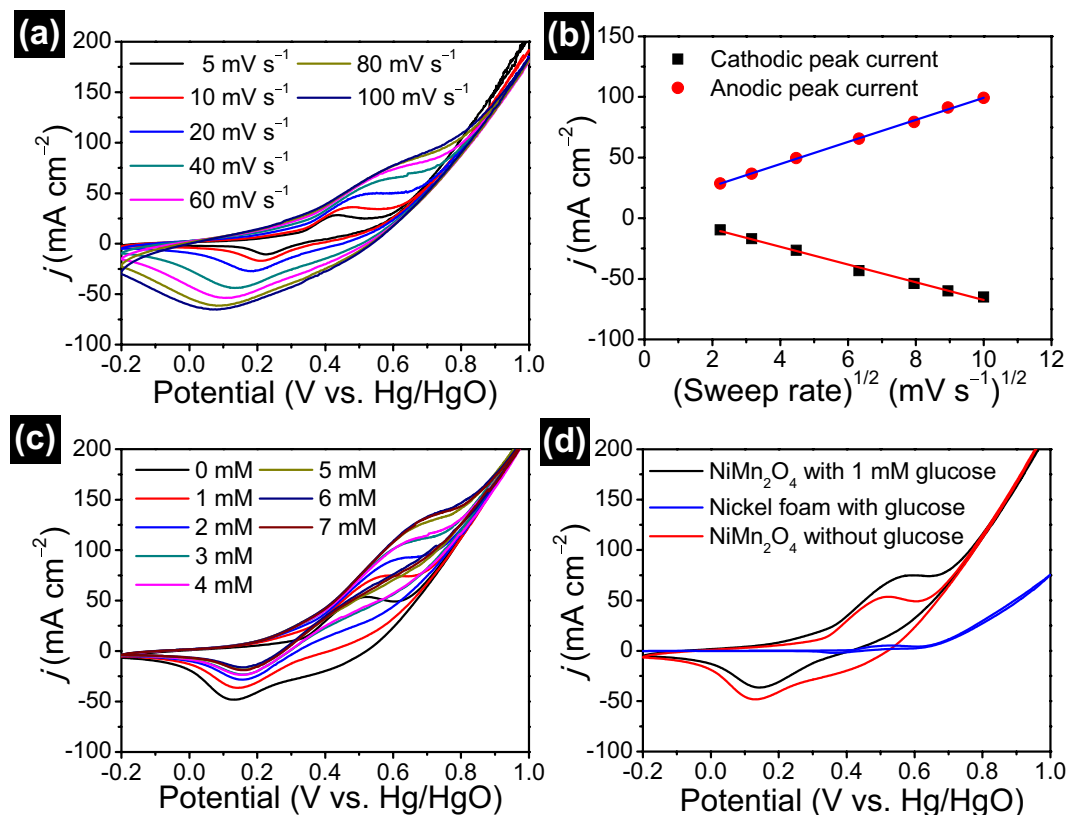
Figure 6. (**a**) CV curves of porous $NiMn_2O_4$ NSs@NF sensor electrode in 0.5 M NaOH electrolyte with 1.0 mM glucose at the sweep rate range from 10 to 100 mV s^{-1}. (**b**) The corresponding fitting curves of anode and cathode peak response currents as a function of the square root of sweep rates. (**c**) CV curves of porous $NiMn_2O_4$ NSs@NF in 0.5 M NaOH electrolyte with concentrations of glucose range from 0 to 7 mM at a sweep rate of 20 mV s^{-1}. (**d**) CV curves of porous $NiMn_2O_4$ NSs@NF and pure nickel foam at the same sweep rate of 20 mV s^{-1} in 0.5 M NaOH electrolyte with 1.0 mM glucose and without 1.0 mM glucose.

sensing performance of porous $NiMn_2O_4$ NSs@NF electrode for glucose. The high current response is attribute to the electroactivity by the large surface area, the outstanding electronic connectivity and the synergy effect of porous $NiMn_2O_4$ nanosheet arrays and nickel foam.

EIS is employed to test the electrochemical impedance property of porous $NiMn_2O_4$ NSs@NF sensor electrode. The electrochemical impedance test is employed in the frequency range from 10^5 Hz to 10^{-2} Hz at 5 mV in a three-electrode cell with 0.5 M NaOH electrolyte solution. Figure S10 shows Nyquist plot of porous $NiMn_2O_4$ NSs@NF electrode. Nyquist plot shows a semicircle at higher frequencies and a long positive-slope line at the lower frequencies. This diameter of semicircle corresponds to the charge transfer resistance, indicating the electron transfer kinetics of the charge transfer process at the working electrode/electrolyte interface[65]. From the inset in Fig. S10, the small diameter of the semicircle reveals the good electric conductivity of porous $NiMn_2O_4$ NSs@NF electrode. At the lower frequencies, this positive-slope line corresponds to the Warburg impedance (Z_w). From Nyquist plot, the slope line with an inclination angle approaching 60° reveals the good diffusion kinetics between the electrode surface and electrolyte[64,66]. The low electrochemical impedance indicates that porous $NiMn_2O_4$ NSs@NF electrode can provide an efficient electron transfer pathway and fast current response for glucose detection.

The amperometric tests are performed to test the electrochemical response property of porous $NiMn_2O_4$ NSs@NF sensor electrode. Under optimal conditions, the amperometric responses are tested at a potential of +0.45 V in 0.5 M NaOH electrolyte solution. Figure 7 shows typical amperometric response curves for various concentrations of glucose. Figure 7a shows the amperometric responses of porous $NiMn_2O_4$ NSs@NF electrode with consecutive step changes of the glucose concentration at a potential of 0.45 V (the concentration range of glucose in electrolyte bath is 0.99–67.30 μM). As can be seen from Fig. 7a, porous $NiMn_2O_4$ NSs@NF electrode shows the good amperometric response at the glucose concentration range from 0.99 μM to 67.30 μM. Figure 7b shows the corresponding fitting curves of the amperometric responses vs. glucose concentrations (the concentration range is 0.99–67.30 μM). The amperometric response increases linearly with the increase of glucose concentration. The linear fitting regression equation is expressed as y (mA cm^{-2}) = 0.01224x + 0.3228 (R^2 = 0.9982). Porous $NiMn_2O_4$ NSs@NF electrode delivers a sensitivity of 12.2 mA mM^{-1} cm^{-2} at the window concentrations of 0.99–67.30 μM. In addition, the limit of detection (LOD) of glucose detection is calculated to be using the following equation[67]. LOD = 3 SD/S, where, S is the slope of the calibration curve (0.01224 mA μM^{-1} cm^{-2}) and SD is the standard deviation of blank (9.9 × 10^{-4} mA cm^{-2}). The detection limit is calculated to be 0.24 μM.
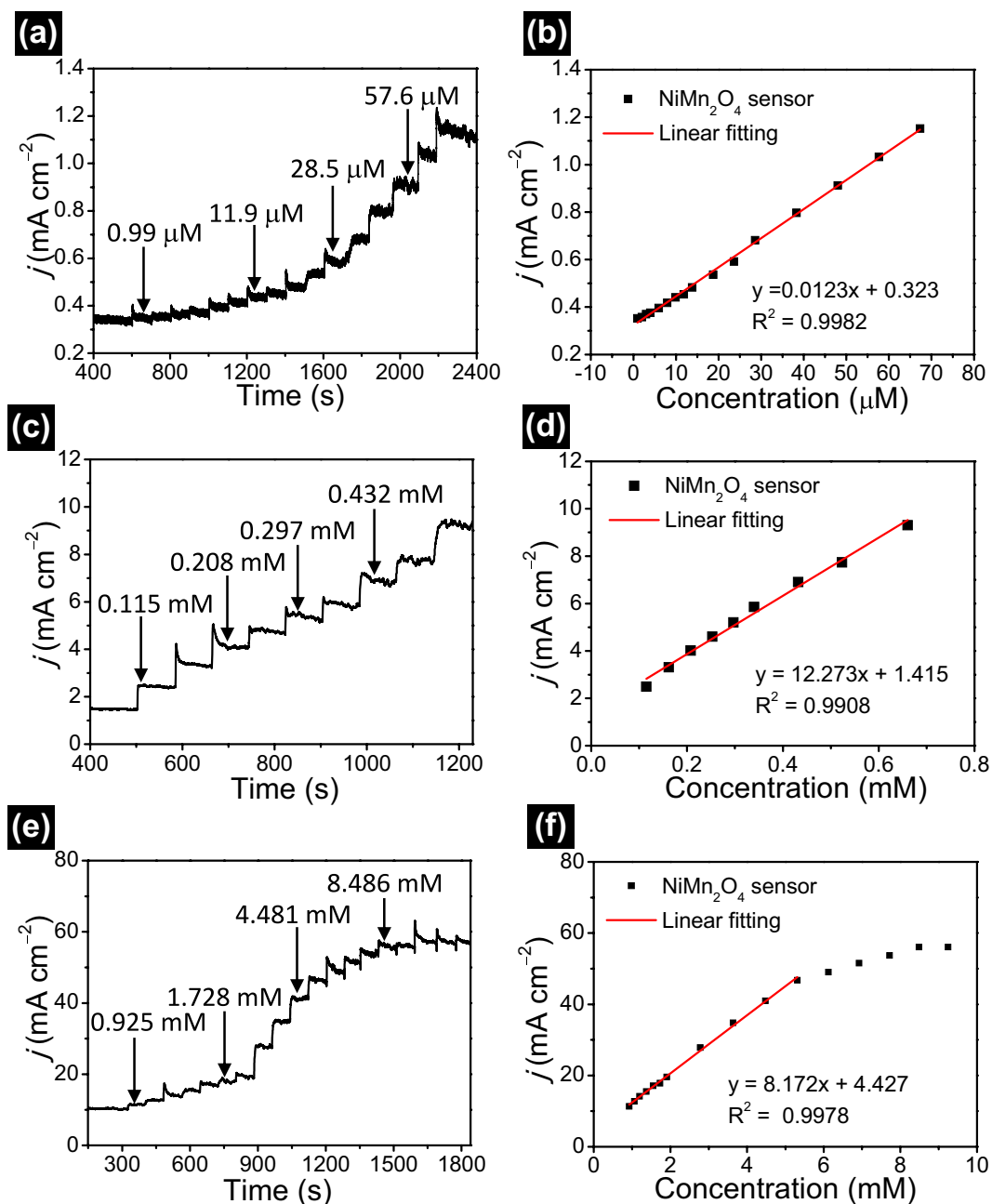
Figure 7. (**a**) The amperometric responses of porous $NiMn_2O_4$ NSs@NF sensor electrode with the successive additions of various concentration of glucose at a potential of 0.45 V (the concentration range of glucose in electrolyte bath is 0.99–67.30 μM). (**b**) The corresponding fitting curves, the concentration range of glucose in electrolyte bath is 0.99–67.30 μM, which shows the sensitivity 12.2 mA mM^{-1} cm^{-2}. (**c**) The amperometric response with the successive additions of various concentration of glucose (the concentration range of glucose in electrolyte bath is 0.115–0.661 mM). (**d**) The corresponding fitting curves, the concentration range of glucose in electrolyte bath is 0.115–0.661 mM, which shows the sensitivity 12.3 mA mM^{-1} cm^{-2}. (**e**) The amperometric response with the successive additions of various concentration of glucose (the concentration range of glucose in electrolyte bath is 0.925–8.486 mM). (**f**) The corresponding fitting curves, the concentration range of glucose in electrolyte bath is 0.067–1.373 mM.

Figure 7c shows the amperometric response of porous $NiMn_2O_4$ NSs@NF electrode with consecutive step changes of the glucose concentration (the concentration range of glucose in electrolyte bath is 0.115–0.661 mM). Similarly, porous $NiMn_2O_4$ NSs@NF electrode shows the good amperometric response at the window concentrations of 0.115–0.661 mM. Figure 7d shows the corresponding fitting curves of the amperometric responses vs. glucose concentrations (the concentration range is 0.115–0.661 mM). The amperometric response increases linearly with the increase of glucose concentration with ranging from 0.115 mM to 0.661 mM. The linear fitting regression equation is expressed as y (mA cm^{-2}) = 12.273x + 1.415 (R^2 = 0.9908). Porous $NiMn_2O_4$ NSs@
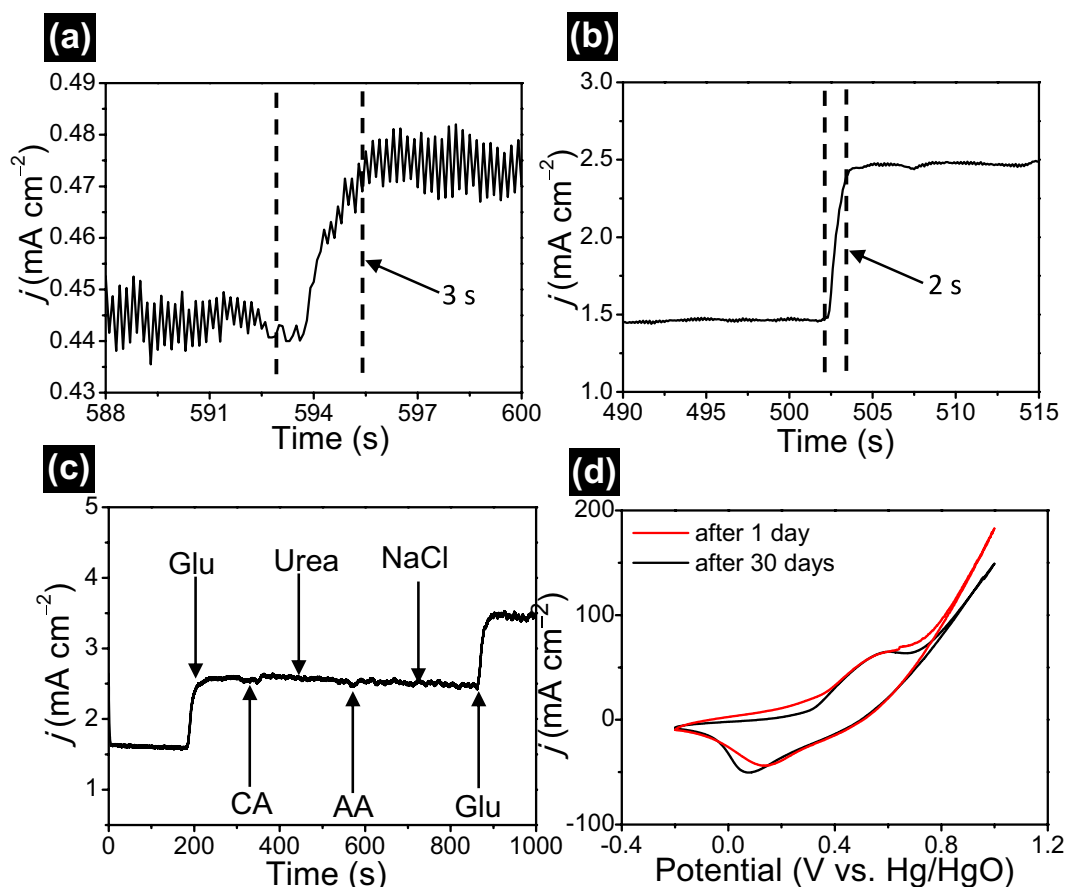
Figure 8. The response time of porous $NiMn_2O_4$ NSs@NF sensor electrode (**a**) A response time of 3 s at a gluconic concentration of 5.964 μM. (**b**) A response time of 2 s at a gluconic concentration of 0.115 mM. (**c**) Amperometric response of porous $NiMn_2O_4$ NSs@NF sensor electrode at 0.45 V upon additions of 1.0 mM glucose, 0.1 mM CA, 0.1 mM Urea, 0.1 mM AA, 0.1 mM NaCl and 0.1 mM Glu in 0.5 M NaOH electrolyte. (**d**) Comparing CV curves of porous $NiMn_2O_4$ NSs@NF sensor electrode after 1 day and 30 days at a sweep rate of 20 mV s^{-1} in 0.5 M NaOH with 1 mM glucose.

NF electrode delivers a sensitivity of 12.3 mA mM^{-1} cm^{-2} at glucose concentration ranging from 0.115 mM to 0.661 mM. Figure 7e shows the amperometric response of porous $NiMn_2O_4$ NSs@NF electrode with consecutive step changes of the glucose concentration (the concentration range is 0.925–8.486 mM). From Fig. 7e, porous $NiMn_2O_4$ NSs@NF electrode still exhibits the good amperometric response at concentration ranging from 0.925 mM to 8.486 mM. Figure 7f shows the corresponding fitting curves (the linear concentration range is 0.925–5.310 mM).

The amperometric response time is crucial parameter for the electrochemical sensor in non-enzymatic glucose detection. The response time of porous $NiMn_2O_4$ NSs@NF electrode is obtained by amperometric measurements in the different glucose concentration in 0.5 M NaOH electrolyte at 0.45 V. Figure 8 presents the response time of porous $NiMn_2O_4$ NSs@NF electrode. With the addition of glucose to electrolyte solution, the glucose oxidation current increases rapidly and then reaches to the steady state. The time begin from the current increase until the current signal to the stead state value is defined as the response time of the sensor. Figure 8a shows an observed response of the sensor is 3 s at a gluconic concentration of 5.964 μM. Figure 8b shows an observed response of the sensor is 2 s at a gluconic concentration of 0.115 mM, which is considered a quick response time. The quick amperometric response time is attributed to good sensibility, excellent electronic conductivity and efficient catalytic ability selectivity of porous $NiMn_2O_4$ NSs@NF electrode. The comparison for the sensing performances of porous $NiMn_2O_4$ NSs@NF electrode and other transition metal oxide materials is listed as shown in Table S1. This comparison table shows the excellent sensing performances of porous $NiMn_2O_4$ NSs@NF electrode compared to the reported sensor.

Anti-interference property of porous $NiMn_2O_4$ NSs@NF sensor electrode is crucial for non-enzymatic electrochemical detection of glucose. It is well-known that saccharides have similar electrochemical reaction behaviors or the interferential behaviors and chloride can lead to the catalyst poisoning to glucose detection. Thus, these compounds cannot be ignored. We investigate the amperometric responses from the other saccharides or chloride such as CA, urea, AA, NaCl in a 0.5 M NaOH electrolyte solution. With the addition of 1.0 mM glucose to the 0.5 M NaOH electrolyte, a distinct response current at 400 s can be observed from Fig. 8c. When upon addition

of other interference compounds such as CA (0.1 mM), urea (0.1 mM), AA (0.1 mM), NaCl (0.1 mM), the current responses cannot be observed or the response current are acceptable and negligible compared to the response current of glucose molecules. With the additions of 1.0 mM glucose, two distinct amperometric responses at 200 s to 900 s can be observed toward glucose detection. The low current responses for other saccharides or chloride indicate that porous $NiMn_2O_4$ NSs@NF have the good selectivity for the electrochemical determination of glucose. Considering that the glucose level is at least 30~50 times higher than those of interfering species in human serum, these interference species produce negligible current responses compared with glucose molecules in a 0.5 M NaOH electrolyte solution[63]. Therefore, these result reveals that porous $NiMn_2O_4$ NSs@NF electrode will be well used toward the detection of glucose in practice.

The long-term stability of porous $NiMn_2O_4$ NSs@NF sensor electrode is examined after 30 days. The stability of porous $NiMn_2O_4$ NSs@NF electrode is measured by CV sweep at 20 mV s^{-1} in 0.5 M NaOH with 1 mM glucose. Figure 8d shows CV curves of porous $NiMn_2O_4$ NSs@NF electrode after 1 day and 30 days. From CV curves, we can observe that no distinct decrease for the peak current after 30-days storage. CV curves almost remains the same shape. In addition, the current response (64.5 mA cm^{-2}) maintains 95.1% of the primitive response (67.8 mA cm^{-2}) after one month storage. These results indicate the excellent electrochemical stability of porous $NiMn_2O_4$ NSs@NF sensor electrode.

Conclusions

In summary, we have successfully fabricated porous $NiMn_2O_4$ NSs@NF sensor electrode *via* a facile hydrothermal reaction followed by a calcination. Porous $NiMn_2O_4$ NSs@NF electrode as non-enzymatic sensor for glucose detection was investigated by the characterizing the structure and electrochemical sensing performances. These porous $NiMn_2O_4$ nanosheets are directly grown on the surface of nickel foam substrate forming porous $NiMn_2O_4$ nanosheet arrays. Owing to the unique porous nanosheet arrays structure, porous $NiMn_2O_4$ NSs@NF electrode possesses large electrochemical active surface area, high electrochemical catalytic activity and fast electron-ion transfer process. The electrochemical tests show that porous $NiMn_2O_4$ NSs@NF as the non-enzymatic sensor electrode for glucose delivers good selective and stable, high sensitivity and reversible and fast response. The porous $NiMn_2O_4$ NSs@NF electrode exhibits the high sensitivity of 12.2 mA mM^{-1} cm^{-2} at a linear window concentrations ranging from 0.99 μM to 67.30 μM and 12.3 mA mM^{-1} cm^{-2} at a linear window concentrations ranging from 0.115 mM to 0.661 mM. The porous $NiMn_2O_4$ NSs@NF electrode also exhibits a low value of LOD (0.24 μM) and a fast response (2 s). These good electrochemical response performances for glucose indicate that porous $NiMn_2O_4$ NSs@NF electrode as non-enzymatic sensing material has the good potential and practical application prospects.

Experimental Section

Reagents. Nickel(II) nitrate hexahydrate ($Ni(NO_3)_2 \cdot 6H_2O$; ≥98.0%), potassium permanganate ($KMnO_4$; ≥99.0%), urea ($CO(NH_2)_2$; ≥99.0%), glucose ($C_6H_{12}O_6 \cdot H_2O$; α_D: +52.5~+53.0°), ascorbic acid ($C_6H_8O_6$, AA; ≥99.7%) and citric acid ($C_6H_8O_7$, CA; ≥99.5%) were purchased and obtained from Tianjin Guangfu Technology Development Co. Ltd.. Hydrochloric acid (HCl, 36.0~38.0%) was obtained and purchased from Jinzhou Ancient City Chemical Reagents Factory. Sodium chloride (NaCl; ≥99.5%) and sodium hydroxide (NaOH; ≥96.0%) were obtained and purchased from Tianli Chemical Reagent Co. Ltd.. Ammonium fluoride (NH_4F; ≥98.0%) was obtained and purchased from Tianjin Fuchen Chemical Reagents Factory. Nickel foam was purchased and obtained from Taiyuan Liyuan Lithium Technology Co. Ltd., more detailed technical parameters of nickel foam were shown in Table S2. De-ionized water (18.3 MΩ cm at 25 °C) was purified and obtained by Milli-Q water system to prepare all solutions. In our work, all chemical reagents and materials were also used without further purification unless otherwise described.

Fabrication of porous $NiMn_2O_4$ NSs@NF electrode. The typical procedure, porous $NiMn_2O_4$ NSs@NF were fabricated via a simple hydrothermal method followed by a heat treatment. Briefly, 2 mmol $Ni(NO_3)_2 \cdot 6H_2O$ (0.582 g), 12 mmol NH_4F (0.444 g) and 30 mmol $CO(NH_2)_2$ (1.800 g) were dissolved into 40 mL deionized water under continuous electromagnetic stirring. A nickel foam (length × width × thickness = 20 mm × 10 mm × 1 mm) was treated and purified with 3 M HCl for 15 min for the remove of the oxide layer on nickel foam. Then, the acid-treated nickel foam was cleaned sequentially by copious amounts of de-ionized water. Then, this pre-treated nickel foam was immersed into above mixed solution. 4 mmol $KMnO_4$ (0.632 g) was dissolved into 40 mL de-ionized water and then was added into the previous solution. After stirring for 30 min, the mixed solution was transferred into a 100 ml-Teflon-lined stainless steel hydrothermal reactor and followed by heating at 110 °C for 8 h. After cooling to the ambient temperature, the precursor was collected and washed with de-ionized water and ethanol thoroughly to remove residual ions. The precursor was dried at 60 °C for 2 h. Finally, the precursor was converted to porous $NiMn_2O_4$ NSs@NF under 350 °C for 2 h and then naturally cooled to the ambient temperature.

Instruments and characterizations. X-ray diffraction (XRD) measurement was carried out using the Rigaku RAD-3C diffractometer instrument (Cu Kα, λ = 1.5405 Å, 35 kV, 20 mA, *2-Theta* angles: 10°–70°). The morphology and structure were investigated by scanning electron microscopy (SEM, JEOL S-4800) under the condition of 3.0 kV operating voltage. Transmission electron microscopy (TEM, JEOL JEM-2100F microscopy) with an energy dispersive X-ray spectroscope (EDS) was also carried out to investigate the element distributions of porous $NiMn_2O_4$ NSs@NF under the condition of 200 kV accelerating voltage. X-ray photoelectron spectroscopy (XPS, ESCALB-MKII250) was performed to analyze the elemental compositions and its valence of porous $NiMn_2O_4$ NSs@NF under a monochromatic 150 W Al Kα source radiation. Nitrogen adsorption/desorption

measurement was performed to analyze the specific surface area of porous $NiMn_2O_4$ NSs@NF on a Micromeritics ASAP 2010 analyzer at 77 K.

Electrochemical measurements. All electrochemical measurements of porous $NiMn_2O_4$ NSs@NF were tested and executed in a three−electrode system cell by an electrochemical workstation (CHI660D, Shanghai, China). In the detecting process, porous $NiMn_2O_4$ NSs@NF was directly used as a sensor electrode. The Hg/HgO electrode with 1 M KOH electrolyte was used as the reference electrode. Platinum plate (length × width × thickness = 20 mm × 20 mm × 0.2 mm) was used as the counter electrode. The 0.5 M NaOH aqueous with different concentration glucose solutions were used as the electrolyte in the electrochemical test process. Cyclic voltammetry (CV), single-potential amperometry and electrochemical impedance spectroscopy (EIS) technologies were carried out to investigate the electrochemical response performances of porous $NiMn_2O_4$ NSs@NF electrode. CV and amperometry measurements were carried out under the magnetic stirring condition of 400 rpm. EIS test was carried out without the stirring condition. All electrochemical measurements were executed at the ambient temperature of 25 °C.

References

1. Guo, Q. *et al*. Flexible and conductive titanium carbide–carbon nanofibers for high-performance glucose biosensing. *Electrochim. Acta* **281**, 517–524 (2018).
2. Justice Babu, K., Sheet, S., Lee, Y. S. & Gnana kumar, G. Three-dimensional dendrite Cu–Co/reduced graphene oxide architectures on a disposable pencil graphite electrode as an electrochemical sensor for nonenzymatic glucose detection. *ACS Sustain. Chem. Eng.* **6**, 1909–1918 (2018).
3. Gopalan, A. I., Muthuchamy, N., Komathi, S. & Lee, K.-P. A novel multicomponent redox polymer nanobead based high performance non-enzymatic glucose sensor. *Biosens. Bioelectron.* **84**, 53–63 (2016).
4. Yoon, H., Xuan, X., Jeong, S. & Park, J. Y. Wearable, robust, non-enzymatic continuous glucose monitoring system and its *in vivo* investigation. *Biosens. Bioelectron.* **117**, 267–275 (2018).
5. Guo, C., Huo, H., Han, X., Xu, C. & Li, H. Ni/CdS bifunctional Ti@TiO₂ core-shell nanowire electrode for high-performance nonenzymatic glucose sensing. *Anal. Chem.* **86**, 876–883 (2014).
6. Bilal, S., Ullah, W. & Ali Shah, A.-U.-H. Polyaniline@CuNi nanocomposite: A highly selective, stable and efficient electrode material for binder free non-enzymatic glucose sensor. *Electrochim. Acta* **284**, 382–391 (2018).
7. Ma, J. L., Yin, B. C., Wu, X. & Ye, B. C. Simple and cost-effective glucose detection based on carbon nanodots supported on silver nanoparticles. *Anal. Chem.* **89**, 1323–1328 (2017).
8. Akhtar, N., El-Safty, S. A., Abdelsalam, M. E., Shenashen, M. A. & Kawarada, H. Radially oriented nanostrand electrodes to boost glucose sensing in mammalian blood. *Biosens. Bioelectron.* **77**, 656–665 (2016).
9. Su, L. *et al*. Colorimetric detection of urine glucose based ZnFe₂O₄ magnetic nanoparticles. *Anal. Chem.* **84**, 5753–5758 (2012).
10. Yang, P. *et al*. NiO/SiC nanocomposite prepared by atomic layer deposition used as a novel electrocatalyst for nonenzymatic glucose sensing. *ACS Appl. Mater. Interfaces* **7**, 4772–4777 (2015).
11. Xiao, F., Li, Y., Gao, H., Ge, S. & Duan, H. Growth of coral-like PtAu-MnO₂ binary nanocomposites on free-standing graphene paper for flexible nonenzymatic glucose sensors. *Biosens. Bioelectron.* **41**, 417–423 (2013).
12. Wang, J. *et al*. Engineered IrO₂@NiO core–shell nanowires for sensitive non-enzymatic detection of trace glucose in saliva. *Anal. Chem.* **88**, 12346–12353 (2016).
13. Li, Y. *et al*. A robust electrochemical sensing of molecularly imprinted polymer prepared by using bifunctional monomer and its application in detection of cypermethrin. *Biosens. Bioelectron.* **127**, 207–214 (2019).
14. Zhang, Y., Jiang, X., Zhang, J., Zhang, H. & Li, Y. Simultaneous voltammetric determination of acetaminophen and isoniazid using MXene modified screen-printed electrode. *Biosens. Bioelectron.* **130**, 315–321 (2019).
15. Sinha, L. *et al*. Hybridization of Co₃O₄ and α-MnO₂ nanostructures for high-performance nonenzymatic glucose sensing. *ACS Sustain. Chem. Eng.* **6**, 13248–13261 (2018).
16. Weina, X., Guanlin, L., Chuanshen, W., Hu, C. & Wang, X. A novel β-MnO₂ micro/nanorod arrays directly grown on flexible carbon fiber fabric for high-performance enzymeless glucose sensing. *Electrochim. Acta* **225**, 121–128 (2017).
17. Tang, Y. *et al*. Fluorescence enhancement of cadmium selenide quantum dots assembled on silver nanoparticles and its application for glucose detection. *Langmuir* **30**, 6324–6330 (2014).
18. Wang, Z. *et al*. Ternary NiCoP nanosheet array on a Ti mesh: a high-performance electrochemical sensor for glucose detection. *Chem. Commun.* **52**, 14438–14441 (2016).
19. Xie, L., Asiri, A. M. & Sun, X. Monolithically integrated copper phosphide nanowire: An efficient electrocatalyst for sensitive and selective nonenzymatic glucose detection. *Sensor Actuat B-Chem* **244**, 11–16 (2017).
20. Xie, F., Cao, X., Qu, F., Asiri, A. M. & Sun, X. Cobalt nitride nanowire array as an efficient electrochemical sensor for glucose and H₂O₂ detection. *Sensor Actuat B-Chem* **255**, 1254–1261 (2018).
21. Xie, F., Liu, T., Xie, L., Sun, X. & Luo, Y. Metallic nickel nitride nanosheet: An efficient catalyst electrode for sensitive and selective non-enzymatic glucose sensing. *Sensor Actuat B-Chem* **255**, 2794–2799 (2018).
22. Manikandan, A. *et al*. Low-temperature chemical synthesis of three-dimensional hierarchical Ni(OH)₂-coated Ni microflowers for high-performance enzyme-free glucose sensor. *J. Phys. Chem. C* **120**, 25752–25759 (2016).
23. Zhu, X., Ju, Y., Chen, J., Liu, D. & Liu, H. Nonenzymatic wearable sensor for electrochemical analysis of perspiration glucose. *ACS sensors* **3**, 1135–1141 (2018).
24. Xue, B., Li, K., Feng, L., Lu, J. & Zhang, L. Graphene wrapped porous Co₃O₄/NiCo₂O₄ double-shelled nanocages with enhanced electrocatalytic performance for glucose sensor. *Electrochim. Acta* **239**, 36–44 (2017).
25. Jiang, D. *et al*. One-step synthesis of three-dimensional Co(OH)₂/rGO nano-flowers as enzyme-mimic sensors for glucose detection. *Electrochim. Acta* **270**, 147–155 (2018).
26. Mao, Y., Mei, Z., Liang, L., Zhou, B. & Tian, Y. Robust and magnetically recoverable dual-sensor particles: Real-time monitoring of glucose and dissolved oxygen. *Sensor Actuat B-Chem* **262**, 371–379 (2018).
27. Li, Y., Niu, X., Tang, J., Lan, M. & Zhao, H. A comparative study of nonenzymatic electrochemical glucose sensors based on Pt-Pd nanotube and nanowire arrays. *Electrochim. Acta* **130**, 1–8 (2014).
28. Zang, G. *et al*. Copper nanowires-MOFs-graphene oxide hybrid nanocomposite targeting glucose electro-oxidation in neutral medium. *Electrochim. Acta* **277**, 176–184 (2018).
29. Xu, H. *et al*. Electrochemical non-enzymatic glucose sensor based on hierarchical 3D Co₃O₄/Ni heterostructure electrode for pushing sensitivity boundary to a new limit. *Sensor Actuat B-Chem* **267**, 93–103 (2018).

30. Jia, L. *et al*. Electrodeposition of hydroxyapatite on nickel foam and further modification with conductive polyaniline for non-enzymatic glucose sensing. *Electrochim. Acta* **280**, 315–322 (2018).

31. Lv, J. *et al*. Facile synthesis of novel CuO/Cu_2O nanosheets on copper foil for high sensitive nonenzymatic glucose biosensor. *Sensor Actuat B-Chem* **248**, 630–638 (2017).

32. Zhang, E., Xie, Y., Ci, S., Jia, J. & Wen, Z. Porous Co_3O_4 hollow nanododecahedra for nonenzymatic glucose biosensor and biofuel cell. *Biosens. Bioelectron.* **81**, 46–53 (2016).

33. Liu, L. *et al*. $NiCo_2O_4$ nanoneedle-decorated electrospun carbon nanofiber nanohybrids for sensitive non-enzymatic glucose sensors. *Sensor Actuat B-Chem* **258**, 920–928 (2018).

34. Yuan, R. *et al*. Coral-like Cu-Co-mixed oxide for stable electro-properties of glucose determination. *Electrochim. Acta* **273**, 502–510 (2018).

35. Huang, J., Wang, W., Lin, X., Gu, C. & Liu, J. Three-dimensional sandwich-structured $NiMn_2O_4$@reduced graphene oxide nanocomposites for highly reversible Li-ion battery anodes. *J. Power Sources* **378**, 677–684 (2018).

36. Ouyang, Y., Feng, Y., Zhang, H., Liu, L. & Wang, Y. Designing sandwiched and crystallized $NiMn_2O_4$@C arrays for enhanced sustainable electrochemical energy storage. *ACS Sustain. Chem. Eng.* **5**, 196–205 (2017).

37. Cella, L. N., Chen, W., Myung, N. V. & Mulchandani, A. Single-walled carbon nanotube-based chemiresistive affinity biosensors for small molecules ultrasensitive glucose detection. *J. Am. Chem. Soc.* **132**, 5024–5026 (2010).

38. Li, Y., Fu, Z. & Su, B. Hierarchically structured porous materials for energy conversion and storage. *Adv. Funct. Mater.* **22**, 4634–4667 (2012).

39. Liu, J., Conry, T. E., Song, X., Doeff, M. M. & Richardson, T. J. Nanoporous spherical $LiFePO_4$ for high performance cathodes. *Energ. Environ. Sci.* **4**, 885–888 (2011).

40. Fan, H. & Shen, W. Gelatin-based microporous carbon nanosheets as high performance supercapacitor electrodes. *ACS Sustain. Chem. Eng.* **4**, 1328–1337 (2016).

41. Ray, A. *et al*. Study on charge storage mechanism in working electrodes fabricated by sol-gel derived spinel $NiMn_2O_4$ nanoparticles for supercapacitor application. *Appl. Surf. Sci.* **463**, 513–525 (2019).

42. Xu, J. *et al*. Fabrication of porous Mn_2O_3 microsheet arrays on nickel foam as high–rate electrodes for supercapacitors. *J. Alloys Compd.* **717**, 108–115 (2017).

43. Renault, N., Baffier, N. & Huber, M. Distribution cationique et distorsion cristalline dans les manganites spinelles $NiCr_xMn_2$-xO_4$. *J. Solid State Chem.* **5**, 250–254 (1972).

44. Larson, E. G., Arnott, R. J. & Wickham, D. G. Preparation, semiconduction and low-temperature magnetization of the system $Ni_{1-x}Mn_{12+x}O_4$. *J. Phys. Chem. Solids* **23**, 1771–1781 (1962).

45. Xing, Z., Ju, Z., Yang, J., Xu, H. & Qian, Y. One-step solid state reaction to selectively fabricate cubic and tetragonal $CuFe_2O_4$ anode material for high power lithium ion batteries. *Electrochim. Acta* **102**, 51–57 (2013).

46. Nagamuthu, S., Vijayakumar, S., Lee, S. H. & Ryu, K. S. Hybrid supercapacitor devices based on $MnCo_2O_4$ as the positive electrode and $FeMn_2O_4$ as the negative electrode. *Appl. Surf. Sci.* **390**, 202–208 (2016).

47. Zhang, Z. *et al*. Formation of hierarchical $CoMoO_4$@MnO_2 core–shell nanosheet arrays on nickel foam with markedly enhanced pseudocapacitive properties. *J. Power Sources* **296**, 162–168 (2015).

48. Liu, X. *et al*. Ni-doped cobalt–cobalt nitride heterostructure arrays for high-power supercapacitors. *ACS Energy Letters*, 2462–2469 (2018).

49. Rao, H. *et al*. Enhanced amperometric sensing using a $NiCo_2O_4$/nitrogen-doped reduced graphene oxide/ionic liquid ternary composite for enzyme-free detection of glucose. *New J. Chem.* **41**, 3667–3676 (2017).

50. An, C. *et al*. Porous $NiCo_2O_4$ nanostructures for high performance supercapacitors via a microemulsion technique. *Nano Energy* **10**, 125–134 (2014).

51. Wang, Y., Wei, X., Li, M., Hou, P. & Xu, X. Temperature dependence of Ni_3S_2 nanostructures with high electrochemical performance. *Appl. Surf. Sci.* **436**, 42–49 (2018).

52. Liu, X. *et al*. Ni_3S_2@Ni foam 3D electrode prepared via chemical corrosion by sodium sulfide and using in hydrazine electro-oxidation. *Electrochim. Acta* **213**, 730–739 (2016).

53. Li, J., Xiong, S., Li, X. & Qian, Y. A facile route to synthesize multiporous $MnCo_2O_4$ and $CoMn_2O_4$ spinel quasi-hollow spheres with improved lithium storage properties. *Nanoscale* **5**, 2045–2054 (2013).

54. Li, L., Hu, H. & Ding, S. Facile synthesis of ultrathin and perpendicular $NiMn_2O_4$ nanosheets on reduced graphene oxide as advanced electrodes for supercapacitors. *Inorg. Chem. Front.* **5**, 1714–1720 (2018).

55. Nguyen, V. H. & Shim, J.-J. Three-dimensional nickel foam/graphene/$NiCo_2O_4$ as high-performance electrodes for supercapacitors. *J. Power Sources* **273**, 110–117 (2015).

56. Han, Y. *et al*. Triple-shelled $NiMn_2O_4$ hollow spheres as an efficient catalyst for low-temperature selective catalytic reduction of NOx with NH_3. *Chem. Commun.* **54**, 9797–9800 (2018).

57. Xu, J. S. *et al*. Fabrication of the porous $MnCo_2O_4$ nanorod arrays on Ni foam as an advanced electrode for asymmetric supercapacitors. *Acta Mater.* **152**, 162–174 (2018).

58. Zhang, W. *et al*. Facile synthesis and electrochemistry of a new cubic rocksalt $Li_xV_yO_2$ (x = 0.78, y = 0.75) electrode material. *J. Mater. Chem. A* **5**, 5148–5155 (2017).

59. Huang, M. *et al*. Facile synthesis of hierarchical Co_3O_4@MnO_2 core–shell arrays on Ni foam for asymmetric supercapacitors. *J. Power Sources* **252**, 98–106 (2014).

60. Ngo, Y.-L. T., Sui, L. J., Ahn, W., Chung, J. S. & Hur, S. H. $NiMn_2O_4$ spinel binary nanostructure decorated on three-dimensional reduced graphene oxide hydrogel for bifunctional materials in non-enzymatic glucose sensor. *Nanoscale* **9**, 19318–19327 (2017).

61. Luo, X. *et al*. Porous $NiCo_2O_4$ nanoarray-integrated binder-free 3D open electrode offers a highly efficient sensing platform for enzyme-free glucose detection. *Analyst* **143**, 2546–2554 (2018).

62. Wang, Y. *et al*. A bifunctional $NiCo_2S_4$/reduced graphene oxide@polyaniline nanocomposite as a highly-efficient electrode for glucose and rutin detection. *New J. Chem.* **42**, 9398–9409 (2018).

63. Xia, K. *et al*. *In situ* fabrication of $Ni(OH)_2$ flakes on Ni foam through electrochemical corrosion as high sensitive and stable binder-free electrode for glucose sensing. *Sensor Actuat B-Chem* **240**, 979–987 (2017).

64. Xu, J. *et al*. Fabrication of hierarchical $MnMoO_4 \cdot H_2O$@MnO_2 core-shell nanosheet arrays on nickel foam as an advanced electrode for asymmetric supercapacitors. *Chem. Eng. J.* **334**, 1466–1476 (2018).

65. Khani, H. & Wipf, D. O. Iron oxide nanosheets and pulse-electrodeposited Ni-Co-S nanoflake arrays for high-performance charge storage. *ACS Appl. Mater. Interfaces* **9**, 6967–6978 (2017).

66. Lin, J. H. *et al*. *In situ* synthesis of vertical standing nanosized NiO encapsulated in graphene as electrodes for high-performance supercapacitors. *Adv. Sci.*, 1700687 (2017).

67. Kumar, T. H. V. & Sundramoorthy, A. K. Non-enzymatic electrochemical detection of urea on silver nanoparticles anchored nitrogen-doped single-walled carbon nanotube modified electrode. *J. Electrochem. Soc.* **165**, B3006–B3016 (2018).

Author contributions

J.Z. and Y.S. performed experiments and electrochemical characterizations, collected and analyzed the data and wrote the main manuscript. X.L. and J.X. conceived the idea and designed the experiments and contributed substantially to revisions. All authors reviewed the manuscript.

Competing interests

The authors declare no competing interests.

Additional information

Supplementary information is available for this paper at https://doi.org/10.1038/s41598-019-54746-2.

Correspondence and requests for materials should be addressed to X.L. or J.X.

Reprints and permissions information is available at www.nature.com/reprints.

Publisher's note Springer Nature remains neutral with regard to jurisdictional claims in published maps and institutional affiliations.